CHARACTERISTIC-BASED NON-LINEAR SIMULATION OF LARGE-SCALE STANDING-WAVE THERMOACOUSTIC ENGINE

Ahmed Abd El-Rahman[1], Ehab Abdel-Rahman*[2]

[1] Assistant Professor, Department of Physics, American University in Cairo
AUC Avenue, 11835 New Cairo, Egypt; Department of the Mechanical
Power Engineering, Cairo University, Giza, Egypt
[2] Associate Professor, Department of Physics, American University in Cairo
AUC Avenue, 11835 New Cairo, Egypt; Director, Yousef Jameel
Science and Technology Research Center
* Corresponding author: ehab_ab@aucegypt.edu

The non-linear interactions between oscillating gas and solid walls in a thermoacoustic stack lead to distorted oscillations, generate viscous and thermal harmonics, cause flow streaming, and influence the saturation amplitude of large-scale thermoacoustic engines. A few linear theories [1–4] and numerical models, based on low-Mach number analysis [5–7], describe the flow dynamics of standing-wave engines, but almost no simulation results are available which enable the prediction of the behavior of engines experiencing large temperature-difference between their stack ends and thus producing large-amplitude oscillations. Here, we report a quasi-one-dimensional non-linear numerical simulation of large-scale standing-wave thermoacoustic engines. The simulation solves the unsteady compressible Euler equations using the mesh method of characteristics. Formulation of the governing equations, implementation of the numerical method and application of the appropriate boundary conditions are presented. The simulation uses an explicit time integration of dynamic equations along with deduced relationships, expressing the friction coefficient and the Stanton number for laminar flow inside circular ducts. The resonator is closed at both ends, Helium is used as the ideal working gas, and the system operates at a mean pressure of 13.8 bars. The stack walls are assumed isothermal while a uniform temperature distribution, with a gradient larger than the corresponding critical onset, is enforced at the gas-solid interface, allowing for the thermoacoustic energy conversion. Hot and cold heat exchangers are ignored for simplicity. The self-induced pressure oscillations are accurately captured in the time domain, and then transferred into the frequency domain using the Cooley-Tukey fast Fourier transform (FFT) algorithm, distinguishing the pressure signals into fundamental and harmonic responses. The results obtained are compared with the Swift [2] experimental work and the linear theory, showing better agreement with the measured values, particularly in the non-linear regime of the dynamic pressure response.

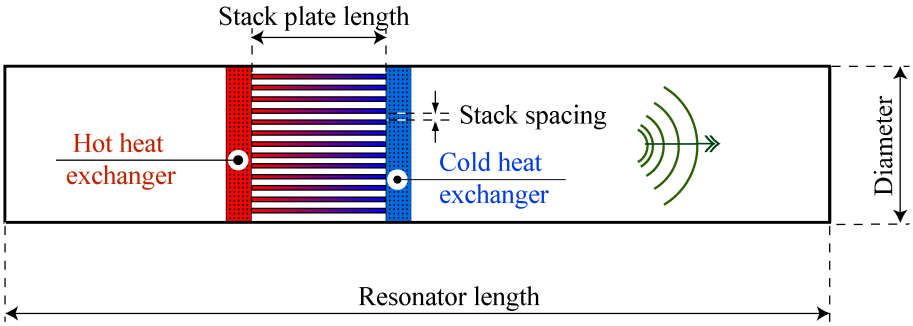

Figure 1: Schematic of a standing-wave thermoacoustic engine having uniform stack parallel plates and two heat exchangers. The engine is closed at one end and loaded at the other end with a linear alternator. The stack porosity ϵ depends on the plate thickness and the inner spacing.

1 Introduction

In a thermoacoustic heat engine, the net thermal energy received by a built-in porous media, which is referred to as the stack in standing-wave devices and the regenerator in traveling-wave layouts, can be effectively converted into sustainable acoustic oscillations and subsequently processed into useful applications. This is functionally achieved by means of a two heat exchangers surrounding the porous media in a long cylindrical resonator and acting as typical heat source and sink of any heat engine. They operate such that a temperature gradient, along the porous media, larger than a critical onset is allowed.

The usefulness of such heat engines lies in their simplicity -no moving parts-, low manufacturing and maintenance cost -porous media usually made of inexpensive ceramic materials- and dependence on environmentally friendly ideal gases as the working fluids. In addition to that, the waste heat and the solar energy can be further integrated as sources of the required input thermal energies. This helps constituting clean and potential means of energy generation and explains the growing interest in understanding, developing and optimizing the performance of thermoacoustic engines. Key challenges include appropriate detection and treatment of non-linear viscous and thermal dissipations.

The well-known Rott approximations and the following developed linear theories [1,2], although advanced, failed to describe the thermoacoustic engine behavior at large pressure ratios pr (ratio of the self-induced acoustic pressure amplitude to its mean value). This was followed by extensive numerical investigations carried out by Worlikar et al. [5, 6]. In his model, he simplified the governing equations into a low-Mach number vorticity-based formulation and was able to treat the widely different length scales encountered in thermoacoustic engines. In his two-dimensional analysis, the stack was made of parallel plates with non-zero thicknesses and the length and width of the computational domain were modified by applying the short stack approximation and assuming periodic boundary conditions.

Latter, Karpov and Prosperetti [8] developed a one-dimensional theoretical model based on the perturbation theory. Growth, non-linear evolution and final saturation of thermoacoustic instabilities, in response of imposed temperature differences, were reported. They were able to model Atchley's prime mover and captured the time dependence behavior of the cold-end dynamic pressure for $\Delta T = 346$ K, however, their results for the pressure amplitude overestimated the corresponding experimental values for the considered conditions. They further extended a non-linear model of thermoacoustic devices [9] which was able to capture some streaming effects. Note that the transition to turbulence has not been clearly elaborated in previous modeling efforts, although suggested by Besnoin [10] in his numerical simulations to appear at large drive/pressure ratios, greater than 6%.

Other numerical attempts have been reported by Hireche et al. [7] and Hamilton et al. [11]. Hireche applied the Worlikar low-Mach number model [5] in his numerical simulation of the idealized thermoacoustic engine. They used the perturbation theory to couple the non-linear two-dimensional flow in the active zone, including the stack and both heat exchangers, with the linear acoustic assumption

in the resonator. Their calculations, although interesting, were time-consuming and did not illustrate the implication of having a "short" thermoacoustic active zone embedded within a long ideal resonator. Also, their recent numerical attempts [12,13] were lacking comparison with practical measurements. To the best of our knowledge, no simulation has been developed which provides adequate prediction of the non-linear characteristics of typical large-amplitude thermoacoustic engines along with their exhibited viscous and thermal harmonics, and shows plausible comparison with practical performance.

Therefore, the objective of this work is to numerically simulate the non-linear large-scale thermoacoustic engines by applying the classical mesh method of characteristics [14] to a simplified version of the unsteady gas dynamics equations. The current results are compared to the experimental measurements of Swift [2], in which Helium is used as the working gas at high mean pressure of 13.8 bars. The analysis below introduces our currently developed mathematical model that solves for the oscillating-flow variables using an explicit Euler-trapezoidal integration scheme while assuming one-dimensional wave propagation. The proposed approach demonstrates the ability of the current numerical tool to accurately predict the general behavior of large-scale engines within reasonable computational time and examine the harmonic content of the self-induced pressure oscillations.

2 Method of Characteristics

The method of characteristics (MOC) is chosen in the present work as the numerical tool. It has the privilege of retaining the non-linear features of the partially-differential governing equations as well as providing an exactly physical path of information exploited by the explicit time integration procedure, as detailed in this section. It also supports an accurate incorporation of the boundaries in terms of their interactions with the oscillating gas.

A MOC-based one-dimensional gas dynamics model is developed and implemented to study the flow field in typical large-scale thermoacoustic engines, and specifically applied here to the Swift [2,3] standing-wave engine for simulation and comparison purposes. This section will first present the conservation equations and then explain the mathematical formulation of the method of characteristics followed by a brief description of the chosen integration scheme and the associated planar wave propagation.

2.1 Conservation Equations

The conservation of mass, momentum and energy equations for quasi one-dimensional unsteady compressible flow can be written, respectively, as follows [14, 15]:

$$\frac{\partial \rho}{\partial t} + \frac{\partial}{\partial x}(\rho u) + \frac{\rho u}{A}\frac{dA}{dx} = 0 \tag{1}$$

$$\frac{\partial}{\partial t}(\rho u) + \frac{\partial}{\partial x}(\rho u^2 + p) + \frac{\rho u^2}{A}\frac{dA}{dx} = -\rho f \tag{2}$$

$$\frac{\partial}{\partial t}\left\{\rho\left(h - \frac{p}{\rho} + \frac{u^2}{2}\right)\right\} + \frac{\partial}{\partial x}\left\{\rho u\left(h + \frac{u^2}{2}\right)\right\} + \frac{1}{A}\left\{\rho u\left(h + \frac{u^2}{2}\right)\right\}\frac{dA}{dx} = \rho q \tag{3}$$

where ρ, u and p are the flow density, x-velocity and pressure, respectively, while h represents the flow specific enthalpy. In this work, they particularly correspond to the *instantaneous* and *local* variations of the oscillating-flow variables, such that neither temporal nor spatial averaging is considered. Also, t, x and A refer to the simulation time, axial coordinate and the duct cross-sectional area, respectively. The effects of wall friction and heat transfer per unit mass of working gas are accounted for by the diffusion terms f and q in the right-hand sides of eqns (1,2), respectively. They were defined by Issa and Spalding [16] in terms of non-dimensional parameters, the friction factor C_f and the Stanton number St:

$$C_f \equiv \frac{1}{4}\frac{fd}{u|u|} \tag{4}$$

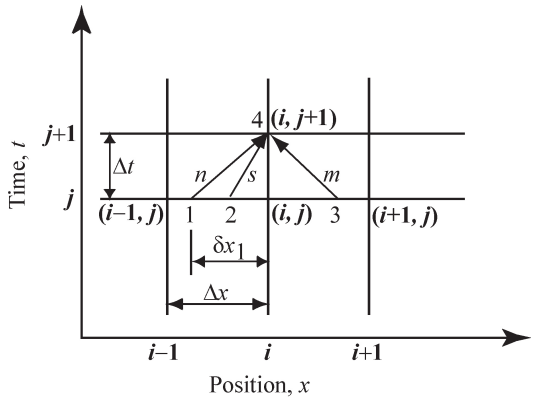

Figure 2: The integration scheme.

$$St \equiv \frac{1}{4}\frac{qd}{C_p\,|u|\,(T_w - T_0)} \tag{5}$$

Here, d is the hydraulic diameter and C_p is the specific heat at constant pressure. T_w and T_0 are the wall and flow stagnation temperatures, respectively. The absolute notation || implies that the value of q "thus, the local instantaneous heat transfer coefficient" is independent on the flow direction, while the sign of f directly varies with the direction of the oscillating-flow velocity such that the corresponding dissipative component $-\rho f$ in the right-hand side of eqn (2) is always resisting the gas motion.

The equation of state closes the set of dynamic equations to be solved numerically using the method of characteristics. To further proceed with the calculations, specific functions of Reynolds number ($Re_d = ud/\nu$), defined in terms of the duct diameter d and instantaneous axial velocity u, are deduced to describe the friction factor and the Stanton number using the data plotted in Fig. 10-1 of Kays and London [17] for a fully developed laminar flow inside circular ducts. The figure plots the friction factor f and the heat transfer coefficient in terms of $StPr^{2/3}$, where Pr is the working gas Prandtl number, as a function of Re on log-log scales and shows quite linear relationships. This assumes a power law relationship in the form of CRe^n, where n is the slope of the line and $\log C$ representing the y-intercept. Accordingly, the following fits are deduced for Helium, Prandtl number of which is 0.67, and implemented in the present mathematical formulation:

$$C_f = 10.1556 Re^{-0.9247} \tag{6}$$

$$St = 1.3289 Re^{-0.7784} \tag{7}$$

2.2 Characteristics Formulation

The characteristics formulation begins with the introduction and substitution of the substantial derivative $S = \partial/\partial t + u\,\partial/\partial x$ into Eqns (1-3). This is followed by the definition of two new differential operators M and N, indicating the variation with time along characteristic lines "representing left- and right-running acoustic waves" of slopes $1/(u-a)$ and $1/(u+a)$, respectively (a is the speed of sound):

$$M \equiv \frac{\partial}{\partial t} + (u-a)\frac{\partial}{\partial x} \tag{8}$$

$$N \equiv \frac{\partial}{\partial t} + (u+a)\frac{\partial}{\partial x} \tag{9}$$

Through mathematical manipulations and considering no change in the ducts' cross-sectional areas -$dA/dx = 0$ in eqns (1-3)-, the partial differential equations are re-written in terms of the Riemann

variables (defined as $m \equiv a - ((\gamma-1)/2)u$ and $n \equiv a + ((\gamma-1)/2)u$) and the entropy s, as follows [14]:

$$M(m) = \left(\frac{\gamma-1}{2}\right)\left[\frac{\gamma}{a}(q+uf)+f\right] - \frac{a^2}{2C_p}\frac{\partial s}{\partial x} \tag{10}$$

$$N(n) = \left(\frac{\gamma-1}{2}\right)\left[\frac{\gamma}{a}(q+uf)-f\right] + \frac{a^2}{2C_p}\frac{\partial s}{\partial x} \tag{11}$$

$$S(s) = \frac{\gamma R}{a^2}(q+uf) \tag{12}$$

γ is the ratio of specific heats. The final partial differential equations are then normalized and finally integrated along the characteristic lines, as shown in Fig. 2. In this calculation, the Euler backward-difference integration scheme is applied to a finite difference grid, leading to the values of m, n and s at each of the nodal points at time $t+\Delta t$ based on their values at time t. Here, the stability criteria, given by the standard Courant-Friedrichs-Lewy condition, is considered to calculate the time incrementation $\Delta t \leq \Delta x/[|u|+a]_{max}$. To explicitly solve for a new time step, linear interpolations are carried out at the characteristics feet, points 1, 2 and 3 in Fig. 2, using the information available at the neighboring grid points:

$$\delta x_1 = \left[\frac{\frac{1}{\Delta t} - (u+a)_{i-1,j}\frac{1}{\Delta x}}{(u+a)_{i,j}} + \frac{1}{\Delta x}\right]^{-1} \tag{13}$$

The integrated MOC variables m, n and s are then converted to familiar terms using the following derived quantities:

$$u = \frac{n-m}{\gamma-1} \tag{14}$$

$$a = \frac{m+n}{2} \tag{15}$$

$$p = \left(\frac{m+n}{2}\right)^{2\gamma/(\gamma-1)} e^{-s} \tag{16}$$

2.3 Trapezoidal Integration

The present integration scheme is a first-order accurate in time and space because of the forward integration time-stepping procedure combined with the spatial linear interpolation at the characteristics feet. Therefore, a second correction step using the trapezoidal method is then introduced. This significantly helps improving the accuracy of the current integration scheme particularly at the first few loading steps by recovering for the relatively coarser grid size, as will be presented in the next section. Thus, the data at point 4 are utilized to recalculate the characteristics slopes and relocate their feet (i.e. at positions 1, 2 and 3). For instance, the new position of point 1 is now defined as:

$$\delta x_1 = \left[\frac{\frac{2}{\Delta t} - \left((u+a)_{i-1,j} + (u+a)_{i,j}\right)\frac{1}{\Delta x}}{(u+a)_{i,j} + (u+a)_{i,j+1}}\right]^{-1} \tag{17}$$

The Riemann variables at the new step (point 4) are then re-evaluated. The integration over the left- and right-running characteristic lines becomes:

$$m_4 - m_3 = \int_3^4 M(m)\,dt \approx \frac{1}{2}\left\{[M(m)]_4 + [M(m)]_3\right\}\Delta t \tag{18}$$

$$n_4 - n_1 = \int_1^4 N(n)\,dt \approx \frac{1}{2}\left\{[N(n)]_4 + [N(n)]_1\right\}\Delta t \tag{19}$$

To proceed with the computational modeling and simulation, a specific FORTRAN program is developed which applies the above-described explicit integration of MOC equations using a Courant number of 0.99 to solve for the conservation equations, discussed in section 2.1. The Swift [2] large-scale

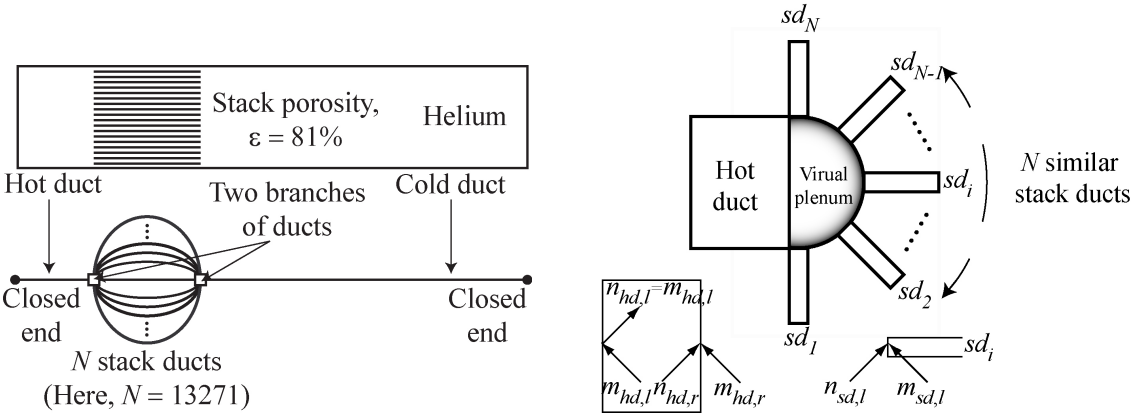

Figure 3: Left: The engine geometry and the corresponding acoustically equivalent duct system with the boundary conditions imposed at the ducts' ends. Right: Illustration of a typical branch of ducts with specified boundary conditions in terms of the Riemann variables m and n. Subscripts: l, r and hd indicate the left and right ends of the hot duct, respectively, while sd refers to the stack ducts. Assuming a rigid wall, $n_{hd,l} = m_{hd,l}$ is enforced at the left end of the hot duct.

thermoacoustic standing-wave engine is considered for comparison purpose.

3 Numerical Model Setup

3.1 Engine Geometry and Meshing

Our motivation in this section is to accurately present an acoustically equivalent duct system to the Swift standing-wave thermoacoustic engine [2] that allows for further comparison of our numerical results to the experimentally-measured dynamic-pressure responses. The engine is made of long cylinder of inner diameter 12.7 cm and length 4.32 cm, filled with Helium at 13.8 bars mean pressure and 303 K mean temperature, and consists of three main segments. In Fig. 3, a 28-cm long hot duct is located at the left end and connected to the hot side of a honeycomb porous media "the stack", which is made of stainless-steel foil with porosity $\epsilon = 81\%$, through a hot heat exchanger. The stack cell has a nominal-size is 1.02 mm but was approximated in the Swift model [2], and currently considered, as made of 1.0 mm-diameter circles. Therefore, the number of stack ducts is $N = 13271$. The third segment follows the opposite cold heat exchanger that is attached to the stack right end and accommodates the rest of the resonator.

For the sake of normalization, reference values of pressure and temperature of 13.8 bars and 303 K, respectively, are considered, while the acoustic velocity, evaluated at the reference temperature, is used to normalize the dynamic velocity "or, the particle oscillating speed". Also, the stack length is used as the length scale. In this 1-D simulation, the engine's computational domain is subdivided in the axial direction into large number of nodes, arranged such that a fixed nodal spacing of $\Delta x = 5$ mm is allowed. Note that for a standing-wave device, the gas particle displacement d_p can be derived in terms of the pressure ratio pr (and thus, the applied thermal load ΔT) and the wave number $k = 2\pi/\lambda$:

$$d_p = \gamma\, pr\, \frac{\lambda}{2\pi} \sin(kx) \tag{20}$$

In the present model, the application of Eqn (20) to the studied range of pressure amplitudes at the fundamental frequencies, leads to particle displacements in the range of $22.0 \le d_p \le 34.0$ mm. This demonstrates the existence of sufficient number of computational nodes within the displacement cycle -Or, the sweep distance of each gas particle- and justifies the adequacy of the chosen grid size $\Delta x = 5$ mm for large pressure ratios $pr \ge 4.0\%$ in capturing the general behavior of the oscillating-flow. Furthermore,

the use of the above grid size, together with the employment of the enhanced trapezoidal integration scheme, provides sufficient accuracy within a reasonable CPU running time for the considered range of the applied thermal load.

3.2 Boundary and Initial Conditions

In the present simulation, the hot duct is thermally insulated and the stack walls are assumed isothermal while a uniform temperature distribution, with a gradient larger than the corresponding critical onset, is enforced at the gas-solid interface, allowing for the thermoacoustic energy conversion. The wall temperature of the cold duct is however maintained fixed at an ambient temperature of 303 K. The engine is assumed to operate at no load and both hot and cold heat exchangers are ignored for simplicity. However, their thermal and viscous influences are introduced in this work by the specification of appropriate values of friction factor $C_f = 0.1$ and Stanton number $St = 0.1$ in eqns (4,5) at their respective axial nodes and at the stack ends.

In these preliminary simulation runs, small pressure perturbations initially prevail the computational domain and the engine is assumed to operate at no load and therefore has two closed ends, at which the inward boundary condition is zero velocity. Thus, by assuming a rigid wall (unity reflection coefficient) at the left end of the hot duct and the right end of the cold duct, this leads to $n_{hd,l} = m_{hd,l}$ and $m_{cd,r} = n_{cd,r}$ respectively, as illustrated in Fig. 3 (right). The figure also shows the implementation of the Benson uniform-pressure model [18] that accounts for the flow behavior in the hot and cold junctions communicating hot and cold ducts to the stack ducts sd_i. His model assumed that the pressure at the end of every duct linked to the junction is the same at any instant and proposed ideal flow behavior "constant entropy level" at junctions [Virtual plenum in Fig. 3]. Benson then applied the conservation of mass and pressure equilibrium to solve for the unsteady compressible flow in a branch of ducts. For instance, the hot-junction inward Riemann variables $m_{hd,r}$ and $n_{sd,l}$ both for the right end of the hot duct and the left end of the stack duct in Fig. 3, respectively, are calculated as:

$$m_{hd,r} = K_{hd}\, n_{hd,r} + \sum_{i=1}^{N} K_{sd_i}\, m_{sd_i,l} - n_{hd,r} \tag{21}$$

$$n_{sd,l} = K_{sd}\, m_{sd,l} + K_{hd}\, n_{hd,r} + \sum_{i=1}^{N-1} K_{sd_i}\, m_{sd_i,l} - m_{sd,l} \tag{22}$$

In the present model, since the entire stack ducts are geometrically similar, experience almost the same physical conditions and exhibit nearly the same flow behavior, this allows us to model the flow in only one duct of the 13271 ducts, while the contribution of all others is reduced at both hot and cold junctions. Therefore, eqns (21,22) become:

$$m_{hd,r} = K_{hd}\, n_{hd,r} + N\, K_{sd}\, m_{sd,l} - n_{hd,r} \tag{23}$$

$$n_{sd,l} = K_{sd}\, m_{sd,l} + K_{hd}\, n_{hd,r} + (N-1) K_{sd}\, m_{sd,l} - m_{sd,l} \tag{24}$$

where

$$K_{hd} = \frac{2A_{hd}}{A_{hd} + \sum_{i=1}^{N} A_{sd_i}} = \frac{2A_{hd}}{(1+\epsilon)A_{hd}} \tag{25}$$

$$K_{sd} = \frac{2A_{sd}}{A_{hd} + \sum_{i=1}^{N} A_{sd_i}} = \frac{2A_{sd}}{(1+\epsilon)A_{hd}} \tag{26}$$

This procedure helps reducing the computational effort sufficiently well as compared with the corresponding running time, consumed by typical computational fluid dynamics (CFD) finite-volume solver packages. Thus, the usefulness of using MOC along with the Benson approach for duct branching is justified. Keeping that in mind, the specification of the nodal entropy variable at the ducts ends and duct junctions becomes necessary to accommodate with the ideal "invariant s" assumption. Therefore, an entropy boundary condition is extended at both ends of the hot and cold ducts, given their respective

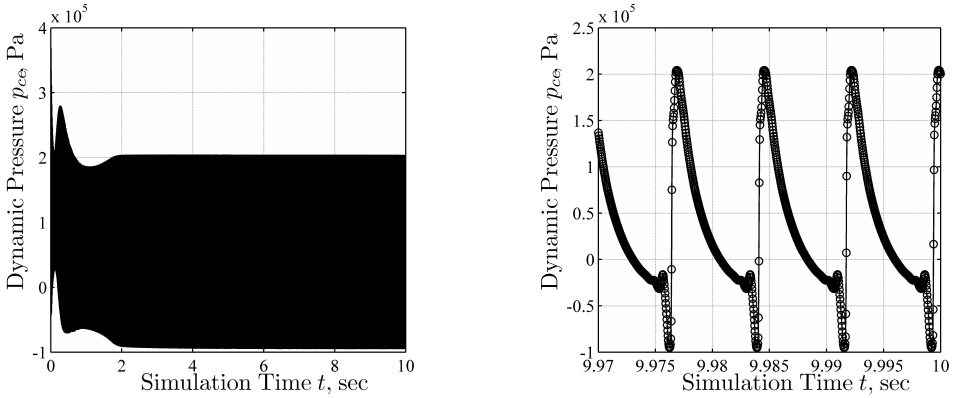

Figure 4: The left figure shows the captured non-linear time evolution of the self-induced pressure oscillations while the right plot illustrates the corresponding distorted waveform at final saturation for an imposed temperature difference $\Delta T = 300$ K. Here, $C_f = 0$ everywhere. A non-zero mean pressure is also predicted.

wall temperatures:

$$s = \frac{2\gamma}{\gamma - 1} \ln a|_{T=T_{wall}} - \ln p \tag{27}$$

4 Planar Wave Propagation and Data Post-Processing

Eriksson [19] studied the higher order mode effects in circular ducts and derived the condition by which the assumption of 1D acoustic flow is preserved. According to his work, the frequency must remain below the cut-on frequency of the first higher order mode, specifically, $f_c \leq 1.841 C_0/\pi d$, where d refers to the inner diameter of the resonator and C_0 is the speed of sound at the reference temperature.

The self-induced pressure oscillations are first recorded in the time domain, and then transferred into the frequency domain, using the Cooley-Tukey fast Fourier transform (FFT). A further analysis of the frequency response reveals the dynamic-pressure fundamental and harmonics components. A special care is necessary for accurate Fourier representation of the steady-periodic temporal signal. A concise technique is carefully developed for this purpose to avoid typical FFT errors, such as aliasing and windowing.

Information about the flow field variables are passed to a post-processing MatLab program that converts the captured non-uniform time series into equally-spaced data sets. This is achieved by first recording a large number of data points -providing sufficient sampling frequency of 1280- to generate a time series which is next trimmed at similar end points "flags" representing the signal peaks, effect of which is similar to windowing effect, to help eliminating the FFT leakage errors. The arithmetic mean is calculated and its value is subtracted from the data points. Then, spline interpolations are carried out to generate uniformly-spaced time series adequately prepared for further FFT processing.

5 Results

Seven simulation runs[1] are conducted at imposed temperature-differences in the range from 260 to 320 degrees Kelvin. Each of these runs represents one loading step. For each ΔT, the simulation is allowed to run for sufficient time until steady-periodic pressure oscillations are obtained. In our simulations, we notice that a total simulation time of ten seconds are necessary for the unsteady behavior to disappear, thus leading the oscillating pressure amplitude to final saturation. Note that the stable time increment

[1] A DELL precision T7500 workstation is used to run the developed serial FORTRAN program. The average CPU time was about ten hours to reach the final saturation.

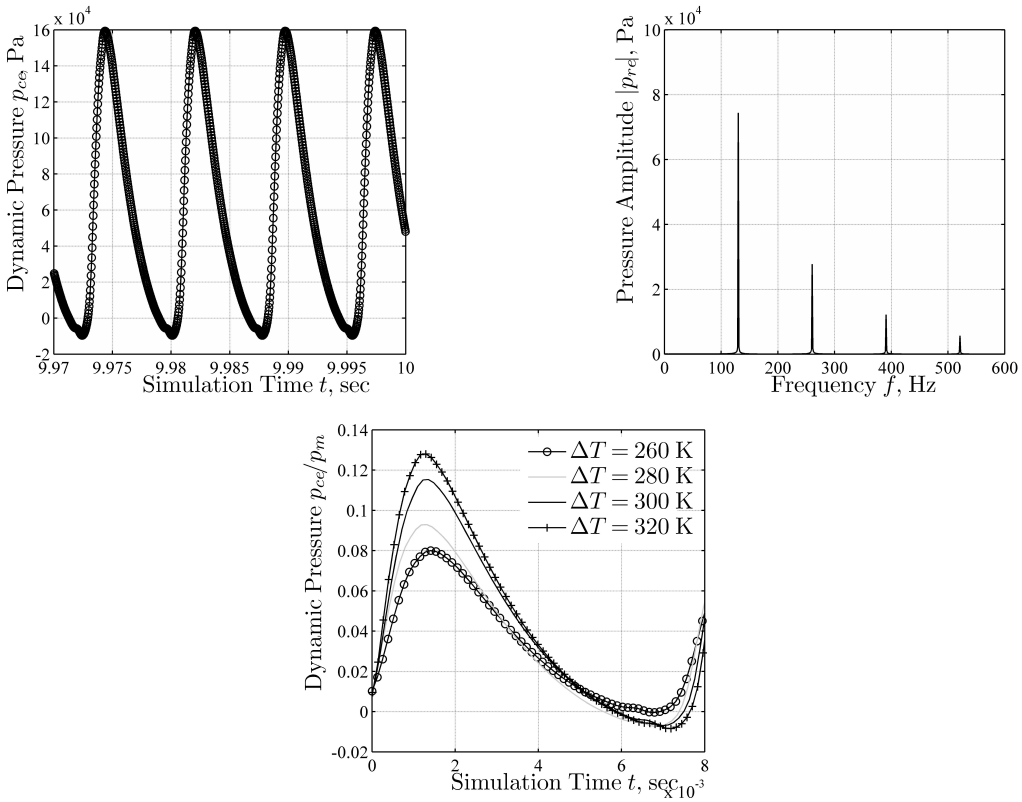

Figure 5: The top left figure shows the captured non-linear time evolution of the self-induced pressure oscillations while the top right plot illustrates the corresponding distorted waveform at final saturation for an imposed temperature difference $\Delta T = 300$ K. A non-zero mean pressure of about 0.74 bars is also predicted. A comparison between the waveforms obtained at different imposed temperature differences is displayed at the bottom, showing their respective distortions.

Δt varies from 2.9×10^{-5} to 3.5×10^{-5} seconds. This represents almost 1/250 of the cycle period based on the fundamental frequency. Pressure values at the engine cold end p_{ce} are recorded once every ten time increments during the last second of the simulation process. Such sampling rate is found appropriate for our current FFT analysis.

Initial *inviscid* simulations are performed to explore the non-linear effect on the oscillating flow behavior and pressure response. The time dependence of the self-induced dynamic pressure p_{ce} is presented in Fig. 4(left) for an applied temperature difference of 300 K between the stack ends, while the right figure shows the waveform of the steady-periodic response. The predicted pressure behavior is clearly non-linear and reveals pressure amplitude of 0.80 bars at the fundamental frequency along with non-negligible pressure harmonics. The figure indicates the existence of nearly shock-wave fronts, partially because the gas particle velocity and the resulting finite-amplitude wave propagation in space are non-linear functions of the gas pressure. This leads to wave distortion as the high pressure zones travel faster than the low pressure ones. Eventually and due to form the ignored viscous effect, the pressure waves steepen to the observed shock-wave fronts. The engine's mean temperature also increases, as expected, as the simulation proceeds because of the imposed thermal load $T_H = 600$ K at the stack hot end. This causes a mean pressure to develop throughout the closed engine space, as indicated in the right figure.

A more realistic behavior is obtained by including the frictional effect through the specification of the laminar friction factor C_f within the flow ducts, according to eqn (6), and at the stack ends using the above specified value $C_f = 0.1$, as plotted in Fig. 5. In contrary to the inviscid results, presented in

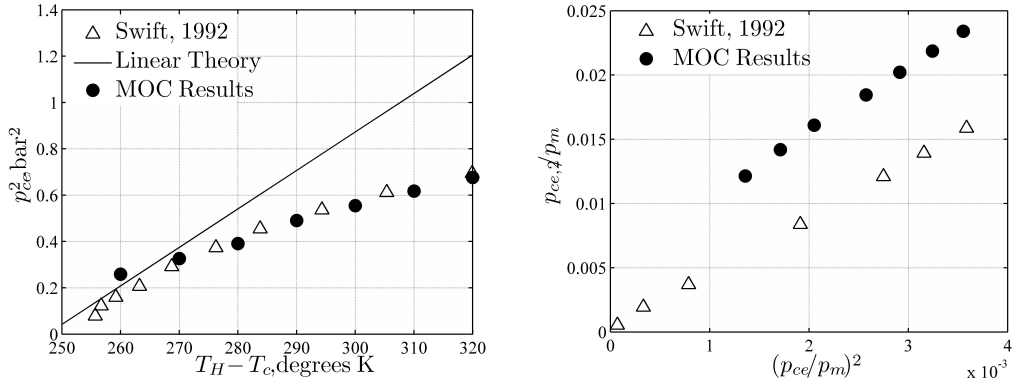

Figure 6: Left: The square of the pressure amplitude at the cold end is plotted versus the temperature differences $T_H - T_c$ between the stack ends. The current MOC results (closed circles) is compared with the measurements of Swift [2] (open triangles) and the corresponding linear theory (solid line). Right: The experimentally-measured first-harmonic amplitude $p_{ce,2}$ as a function of the fundamental amplitude of the oscillating pressure. Both values are normalized by the *initial* system mean-pressure 13.8 bars. Here, the maximum pressure ratio $p_{ce}/p_m \approx 6\%$.

Fig. 4, the current wave fronts smooth out and the corresponding pressure amplitude at the fundamental frequency has decreased by a factor of 8%. An FFT of the captured steady temporal solution is then processed to distinguish the fundamental response and the harmonic content, as indicated in Fig. 5. Our calculations predict the fundamental frequency $f_o = 130.3$ Hz, whereas the measured value falls in the range of $120 - 125$ Hz. One possible reason for such discrepancy is the one-dimensional approximation used to model the standing-wave engine space and the omission of the two heat exchangers. The top right figure introduces the first three harmonics developed within the engine as the non-linear simulation proceeds. Here, the amplitude p_{ce} at the fundamental frequency is 2.68 times the amplitude $p_{ce,2}$ at twice the fundamental frequency. This closely matches the 1/3 ratio reported by Swift [2] and further updated by Olson and Swift [3].

A comparison is also presented at the bottom figure showing the relative behaviors, in terms of the normalized pressure distortions, at different stack-ends temperature differences. The higher the temperature difference, the greater the pressure distortion. The mean pressure is observed to increase as well. Pressure and temperature distortions are expected to decrease the thermoacoustic heat pumping along the stack plates, and thus lower the engine thermal efficiency. The simulation results indicate that the generated pressure amplitude at the fundamental frequency falls in the range of $0.53 - 0.8$ bars. The pressure ratios are calculated in the range of $3.8 - 6\%$.

Figure 6 compares the current one-dimensional non-linear simulation results, based on the mesh method of characteristics, to both experimental values and linear theory. The square of the dynamic pressure is plotted as a function of the imposed thermal load in terms of the temperature difference $\Delta T = T_H - T_c$ between the stack ends. Note that the linear theory does not exactly derive the plotted linear dependence of the self-induced pressure-oscillations on the resulting temperature difference. However and for the sake of comparison, this dependence accounts for the linear relationship between the corresponding amount of heat input Q_H that would have been added to produce the referred dynamic pressure values. Generally, the current acoustic results show better agreement with the Swift measured values, compared to linear theory, as indicated in Fig. 6(right), in the range of ΔT from 270 to 320 degrees.

To help illustrating the harmonic content of the captured pressure signal at the engine's cold end, Fig. 6 plots the variation of the pressure amplitude $p_{ce,2}$ at twice the fundamental frequency with that calculated at the fundamental frequency p_{ce}. This is also shown in comparison with the Swift measured values. The current numerical predictions overestimate the harmonic content by about 30%, as indicated. However, we believe that the dominant mechanism that affects the magnitude of the pressure

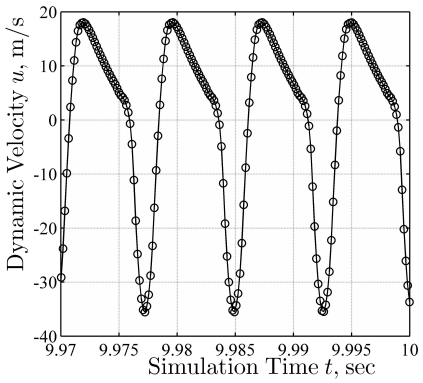

Figure 7: The oscillating velocity at a point located midway between the two engine's closed ends at an initial operating mean pressure and temperature of 13.8 bars and 303 K, respectively. The imposed temperature difference is $\Delta T = 300$ K. Notice the non-zero mean velocity indicating the existence of the non-linear flow streaming within the engine.

harmonics is the geometrical discontinuities leading to definite complex and multi-dimensional flow behavior which is not considered in the present model. This explains the use of inserts, as suggested by Swift [2], to break down the induced harmonics and minimize the succeeding acoustic power dissipation. Also, this could be possibly due to the inability of employed grid size in detecting the pressure harmonics in an accurate way as that of the corresponding fundamental pressures. Nevertheless, the present model provides a useful numerical tool that can be used to predict the general flow behavior within large-scale thermoacoustic devices consuming a reasonable computational effort.

In addition to the aforementioned results on the captured dynamic pressure at the engine's cold end, our developed FORTRAN program solves for the one-dimensional time-dependent acoustic velocity within the engine at every instant "or, time incrementation" using eqn (14) and allows us to trace its history at a point located in the middle of the engine "velocity anti-node" where the dynamic velocity is expected to peak. The generated velocity oscillations are shown in Fig. 7. The acoustic wave is clearly distorted because of the nonlinearity which is typically characterizing large-amplitude thermoacoustic devices. Here, a negative mean velocity within the cold duct is noticed indicating the existence of the gas flow streaming towards the stack cold end.

6 Conclusions

A new characteristic-based numerical scheme is specifically developed which enables accurate modeling and simulation of the non-linear oscillations existing in large-scale thermoacoustic engines. The developed mathematical model solves for the 1D unsteady Euler compressible equations with specific definitions for the wall heat transfer and frictional effect. The numerical simulation assumes isothermal stack plates and applies the Benson [18] uniform-pressure model at the stack ends to account for the flow behavior within the duct junctions. The evolving acoustic pressure and velocity signals are captured and the resulting FFT pressure amplitudes reveals better agreement with experimental values [2], as compared to the linear theory.

References

[1] G. W. Swift. Thermoacoustic engines. *The Journal of the Acoustical Society of America*, 84(4):1145–1180, 1988.

[2] G. W. Swift. Analysis and performance of a large thermoacoustic engine. *The Journal of the Acoustical Society of America*, 92(3):1551–1563, 1992.

[3] J. R. Olson and G. W. Swift. Similitude in thermoacoustics. *The Journal of the Acoustical Society of America*, 95(3):1405–1412, 1994.

[4] G.W. Swift and Acoustical Society of America. *Thermoacoustics: A Unifying Perspective for Some Engines and Refrigerators*. AIP Conference Proceedings / Atomic, Molecular, Chemical Physics Series. Acoustical Society of America through the American Institute of Physics, 2002.

[5] Aniruddha S. Worlikar and Omar M. Knio. Numerical simulation of a thermoacoustic refrigerator: I. unsteady adiabatic flow around the stack. *Journal of Computational Physics*, 127(2):424 – 451, 1996.

[6] Aniruddha S. Worlikar, Omar M. Knio, and Rupert Klein. Numerical simulation of a thermoacoustic refrigerator: Ii. stratified flow around the stack. *Journal of Computational Physics*, 144(2):299 – 324, 1998.

[7] Omar Hireche, Catherine Weisman, Diana Baltean-Carlès, Maurice François, Patrick Quéé, and Luc Bauwens. Numerical model of a thermoacoustic engine. *Canadian Acoustics*, 36(3), 2008.

[8] S. Karpov and A. Prosperetti. Nonlinear saturation of the thermoacoustic instability. *The Journal of the Acoustical Society of America*, 107(6):3130–3147, 2000.

[9] Sergey Karpov and Andrea Prosperetti. A nonlinear model of thermoacoustic devices. *The Journal of the Acoustical Society of America*, 112(4):1431–1444, 2002.

[10] Etienne Besnoin and Omar M. Knio. Numerical study of thermoacoustic heat exchangers. *Acta Acustica united with Acustica*, 90(3):432–444, 2004.

[11] Mark F. Hamilton, Yurii A. Ilinskii, and Evgenia A. Zabolotskaya. Nonlinear two-dimensional model for thermoacoustic engines. *The Journal of the Acoustical Society of America*, 111(5):2076–2086, 2002.

[12] Omar Hireche, Catherine Weisman, Diana Baltean-Carles, Patrick Le Quere, and Luc Bauwens. Low mach number analysis of idealized thermoacoustic engines with numerical solution. *The Journal of the Acoustical Society of America*, 128(6):3438–3448, 2010.

[13] Omar Hireche, Catherine Weisman, Diana Baltean-Carlès, Patrick Le Quéré, Maurice-Xavier François, and Luc Bauwens. Numerical model of a thermoacoustic engine. *Comptes Rendus Mécanique*, 338(1):18 – 23, 2010.

[14] J.A.C. Kentfield. *Nonsteady, one-dimensional, internal, compressible flows: theory and applications*. Oxford engineering science series. Oxford University Press, 1993.

[15] D.E. Winterbone and R.J. Pearson. *Design techniques for engine manifolds: wave action methods for IC engines*. Professional Engineering Pub. Limited, 1999.

[16] R. I. Issa and D. B. Spalding. Unsteady one-dimensional compressible frictional flow with heat transfer. *Journal of Mechanical Engineering Science*, 14(6):365–369, 1972.

[17] W.M. Kays and A.L. London. *Compact heat exchangers*. Krieger Pub. Co., 1984.

[18] R. S. Benson. Research note: A simple algorithm for a multi-pipe junction in non-steady homentropic flow. *Journal of Mechanical Engineering Science*, 17(1):40–44, 1975.

[19] L. J. Eriksson. Higher order mode effects in circular ducts and expansion chambers. *The Journal of the Acoustical Society of America*, 68(2):545–550, 1980.